One-dimensional image reconstruction by exponential filtering in infrared stellar speckle interferometry: application to IRC +10216

Rafael Navarro

Instituto de Optica "Daza de Valdés," Serrano 121, 28006 Madrid, Spain

Domingo Benítez

Universidad Politécnica de las Palmas, Las Palmas de Gran Canaria, Spain

F. Javier Fuentes

Instituto de Astrofísica de Canarias, 38200 La Laguna, Tenerife, Spain

Received May 22, 1989; accepted October 18, 1989

Exponential filtering, together with an improved version of the iterative Fourier-transform algorithm, is applied to image reconstruction from one-dimensional infrared stellar speckle interferometry data. The performance of the method is checked first by computer simulations with both noiseless and noisy data and then with a realistic simulation of one-dimensional infrared stellar speckle interferometry. We have seen no problems with convergence. The only problem that we found was an expected noisy appearance of the results when noisy data were simulated. Finally, the method was applied to observational specklegrams of the infrared source IRC +10216, in two standard photometric bands: K and M (2.2 and 5 μm, respectively). The reconstruction in K of a north–south scan clearly shows three components inside a circumstellar shell. On the other hand, in the M band only a wing on the north side of the main component is resolvable.

1. INTRODUCTION

The problem of reconstructing an image from its power spectrum appears in different fields of physics, such as x-ray diffraction and high-resolution astronomy. Stellar speckle interferometry[1] (SSI) is probably the most widely applied high-resolution technique in astronomy, since it gives useful results, mainly in resolving binary stars (see Ref. 2 for an interesting review of this subject). The image-reconstruction problem appears here because SSI provides the power spectrum $|F(\mathbf{u})|^2$ of the object intensity $o(\mathbf{x})$ with respect to the cutoff frequency of the telescope but at the cost of missing the phase $\phi(\mathbf{u})$ of the Fourier transform (FT) of $o(\mathbf{x})$ ($\mathbf{x}$ and $\mathbf{u}$ are vectors). Therefore the attempt to recover the object intensity by an inverse FT of the power spectrum will give the object intensity autocorrelation $Q(\mathbf{x})$ instead of $o(\mathbf{x})$. The phase problem, which appears in reconstruction of the object, consists of finding the phase $\phi(\mathbf{u})$ of $F(\mathbf{u})$ by knowing the modulus $|F(\mathbf{u})|$ and some constraints on $o(\mathbf{x})$, usually its finite extent and that the intensity is a real nonnegative magnitude.

It has been shown[3,4] that this general problem can be unambiguously solved in two dimensions, except for a trivial 180° rotation of the object. However, Walther[5] had proved the lack of uniqueness in the one-dimensional (1-D) phase problem. In fact, he showed that there exist 2^N different solutions that are compatible with the same data [N being approximately the number of effective sampling points of $|F(\mathbf{u})|$]. Such ambiguity can be removed by using additional information. One possible way to overcome this difficulty (apart from techniques that prevent phase loss, such as the Knox–Thompson[6] and the triple-correlation[7] methods) is to take two different intensity measurements. In this way, Walker[8,9] has proposed exponential filtering as a method to obtain a second intensity measurement compatible with SSI. The exponential filter $g(x) = \exp(\alpha x)$, when applied to every short-exposure speckle image, gives, after a corresponding second SSI procedure, an apodized version of the power spectrum $|F'(\mathbf{u})|^2 = |F(\mathbf{u}) * G(u)|^2$, which constitutes the second intensity measurement. Then the ambiguity of the reconstruction (even the 180° uncertainty) can be totally removed by using both power spectra, $|F(\mathbf{u})|^2$ and $|F'(\mathbf{u})|^2$.

In this paper we study the performance of exponential filtering for application to image reconstruction from 1-D infrared SSI data. First we describe a modified version of the Walker[9] algorithm (Section 2). In Sections 3 and 4 the performance of this algorithm is checked with both noiseless and noisy data, including a realistic computer simulation of 1-D infrared SSI. Finally (Section 5), the method is applied to high-resolution observations of the source IRC + 10216 in the K and M photometric bands (2.2 and 5 μm, respectively); good-quality reconstructions that show some new features of this source are obtained.

2. EXPONENTIAL FILTERING AND MODIFIED WALKER ALGORITHM

As we mentioned above, exponential filtering in SSI is a method that yields two intensity measurements. This permits us to avoid ambiguities in solving the subsequent phase

0740-3232/90/030459-09$02.00

problem. The SSI consists of recording a set of short-exposure images, or frames, $i_k(\mathbf{x})$ of the object $o(\mathbf{x})$. Each image depends on the instantaneous atmospheric configuration

$$i_k(\mathbf{x}) = o(\mathbf{x}) * p_k(\mathbf{x}), \tag{1}$$

where $p_k(\mathbf{x})$ is the instantaneous point-spread function (PSF) corresponding to the kth configuration of the atmosphere (and telescope) and $*$ means convolution. In conventional imagery one averages the frames, getting $\langle i_k(\mathbf{x})\rangle$, the resulting image. In SSI, instead, one averages the power spectra:

$$\langle |I_k(\mathbf{u})|^2\rangle = |F(\mathbf{u})|^2 \langle |P_k(\mathbf{u})|^2\rangle, \tag{2}$$

where capital letters have been used for the FT's of i_k and p_k. Then, taking the average power spectrum of a point reference star, one can solve Eq. (2) to obtain the power spectrum of the object, $|F(\mathbf{u})|^2$, with respect to the cutoff frequency of the telescope.[2] This single intensity measurement does not guarantee the uniqueness of the phase problem in the 1-D case. One way to obtain a second intensity measurement (optionally from the same short-exposure data) is by exponential filtering.[8,9] Exponential filtering consists in multiplying every frame $i_k(\mathbf{x})$ by an exponential filter $g(x) = \exp(\alpha x)$, with $0.5 \le \alpha L_x \le 2$ (L_x being the x length of the images in pixels). In this way one obtains a second set of speckle images and can repeat the SSI procedure to obtain the second intensity measurement (an apodized version of the power spectrum). Walker[8] has shown that the exponential filter has the distributive property with respect to the convolution, which allows us to write

$$i'_k(\mathbf{x}) = [o(\mathbf{x}) * p_k(\mathbf{x})]g(x) = [o(\mathbf{x})g(x)] * [p_k(\mathbf{x})g(x)] \tag{3}$$

or, in another form, $i'_k(\mathbf{x}) = o'(\mathbf{x}) * p'_k(\mathbf{x})$, where primes mean filtered images. It follows that Eq. (2) also applies, in the same way, to the filtered spectra:

$$\langle |I'_k(\mathbf{u})|^2\rangle = |F'(\mathbf{u})|^2 \langle |P'_k(\mathbf{u})|^2\rangle. \tag{4}$$

As a consequence, the second intensity measurement is obtained by solving Eq. (4). The exponential filter causes a redistribution of the energy (mainly by introducing a sort of anisotropy in the images). One way to obtain unambiguous reconstruction is to use the two spectra $|F|$ and $|F'|$ as the input data in algorithms such as that of Fienup[10] or simulated annealing,[11] by introducing appropriate modifications.

Walker[9] proposed the use of a modified version of the Fienup[10] error-reduction algorithm. The modification was to change the input data at each iteration from the previous one. In this way, $|F(\mathbf{u})|$ is the input for the odd iterations (note that in this case there is no difference with respect to the Fienup algorithm), whereas $|F'(\mathbf{u})|$ is used in the even iterations. After each iteration the current guess, $o(\mathbf{x})$, is transformed into $o'(\mathbf{x})$, or vice versa, by multiplying or dividing by the exponential filter, according to the type of data to be used in the next iteration. The same basic scheme is applicable to the incorporation of exponential filtering to any iterative image-reconstruction algorithm.

Apart from the application of exponential filtering to 1-D data, we have incorporated a new modification of the Walker algorithm. It consists of the combined use of both versions of the original Fienup algorithm: the error-reduction (ER) version and the hybrid input–output (HIO) version. The main difference between the two versions is in the method of imposing the constraints.[10,12] In the ER algorithm, those pixels used in the current guess that do not satisfy the constraints are forced to be zero. On the other hand, in the HIO version those pixels are changed by a linear combination of the input and output guesses (we have used the feedback constant $\beta = 0.7$). The constraints are imposed in both odd (unfiltered data) and even (filtered data) iterations, in the latter case after division by the exponential filter. We have found a strong improvement in the convergence of the algorithm when the combination of the two versions was used. To compute the degree of convergence, we used the Fienup cost function for the object domain[13]:

$$E_0 = \left[\sum\sum_{(i,j)\in\Gamma} |g^k_{i,j}|^2 \Big/ \sum\sum_{i,j} |g^k_{i,j}|^2\right]^{1/2},$$

where $g^k_{i,j}$ is the kth object estimate (before imposition of the constraints) in the pixel (i, j) and Γ is the set of pixels at which $g^k_{i,j}$ violates the object-domain constraints. After an initial cycle of ER only, composed of 40–50 iterations, the algorithm completes a few (1–4) hybrid cycles, each consisting of 20–40 HIO iterations followed by 10 ER iterations. This is usually sufficient for a good solution in the 1-D case. However, several cycles can be required when the data are noisy. The parameter α of the exponential filter has a great influence on the convergence of the algorithm. Although we have not found a unique optimum value, as the length of the image L_x increases, the product αL_x should be closer to 2, in order to optimize the result. The algorithm was also tested in two dimensions, resulting in the same behavior as that of the Fienup algorithm, except that exponential filtering gave the correct orientation of the object (reconstructions were approximately equal to those shown in Ref. 11). All reconstructions shown below could be obtained only by the combined use of the ER and HIO versions of the algorithm, whereas the original Walker algorithm stagnates in the great majority of cases.

3. PERFORMANCE OF THE ONE-DIMENSIONAL MODIFIED WALKER ALGORITHM

In phase-retrieval or image-reconstruction problems it is usual to check the performance of the algorithms and methods with known data before applying them to unknown cases. This is the only way, in general, to be certain about the behavior of the methods and the validity of the results. In this section we check the performance of the modified 1-D Walker algorithm with computer-simulated data of increasing difficulty: first with noiseless data and then with increasing amounts of noise added to the data.

A. Reconstructions from Noiseless Data

In this section we compute the apodized spectrum by directly multiplying the object by the exponential filter and then compute the FT of the result. Objects with 32 to as many as 300 pixels were tested. Also, two different input guesses for each object were used: constant and random pixels. In all noiseless reconstructions the algorithm has shown a good convergence within a single cycle, which lowers the cost

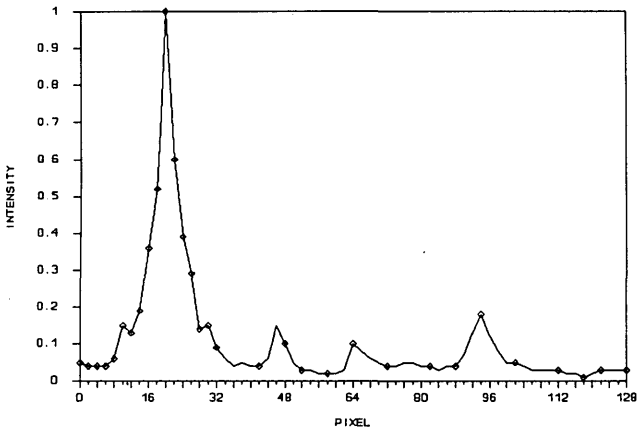

Fig. 1. Exponential filtering 1-D reconstruction from noiseless data (continuous curve). The original object (symbols) is 128-pixel-wide, central row of a CCD image of the M51 galaxy (bias and background have been subtracted).

function from an initial value of the order of 10^{-1} to roughly 10^{-5} (4 orders of magnitude). It should be noted that such a value of the final cost function is of the same order of magnitude as the computing errors of our fast-Fourier-transform algorithm. In consequence, we can consider that a value close to the absolute minimum of the cost function has been found in all noiseless cases. Figure 1 shows the original 128-pixel object (symbols) and its reconstruction (continuous curve): a 1-D central row of a charge-coupled device (CCD) image of the galaxy M51 (background and bias have been removed here). The parameter of the exponential filter was $\alpha = 0.015$. The algorithm was composed of 50 ER, 20 HIO, and 10 ER iterations. This used ~10 sec of CPU time in a Data General Eclipse MV10000 computer. The reconstruction shows no appreciable difference from the original. All noiseless reconstructions showed the same results. This means that in our tests we found no problems of convergence or stagnation for object sizes up to 300 pixels. The algorithm shows a uniform, good, and fast convergence independently of the structure of the object or of the input guess. This behavior is quite different from that observed in two-dimensional (2-D) objects. In 2-D reconstructions the algorithm presented stagnation problems in many cases. 2-D results were mostly the same as those found by Nieto-Vesperinas *et al.*[11] with the Fienup algorithm. This fact is certainly due to the number of trapping minima of the cost function, which is roughly 2^N (N being proportional to the total number of pixels). Then, even for small 2-D objects (32×32 pixels), the number of trapping minima is much greater than for the 300-pixel 1-D object. The exponential filtering and the modified Walker algorithm seem to guarantee not only uniqueness but also convergence when applied to noiseless 1-D object reconstruction.

B. Reconstructions from Noise Data

Once the performance of the method has been checked with noiseless data, the next step is to add increasing amounts of noise to the data. The noise is introduced by adding Gaussian distributed random numbers, with zero mean, to each pixel of both spectra (with and without apodization). Here an average signal-to-noise-ratio (SNR) was used to compute the standard deviation of the random numbers: the mean SNR was defined as the average value, within all pixels, of the spectrum divided by the standard deviation of the noise. Then the exponential filtering was tested for decreasing average SNR (SNR = 20, 10, 5). Figure 2 shows reconstructions (continuous curves) of the object in Fig. 1 (dashed

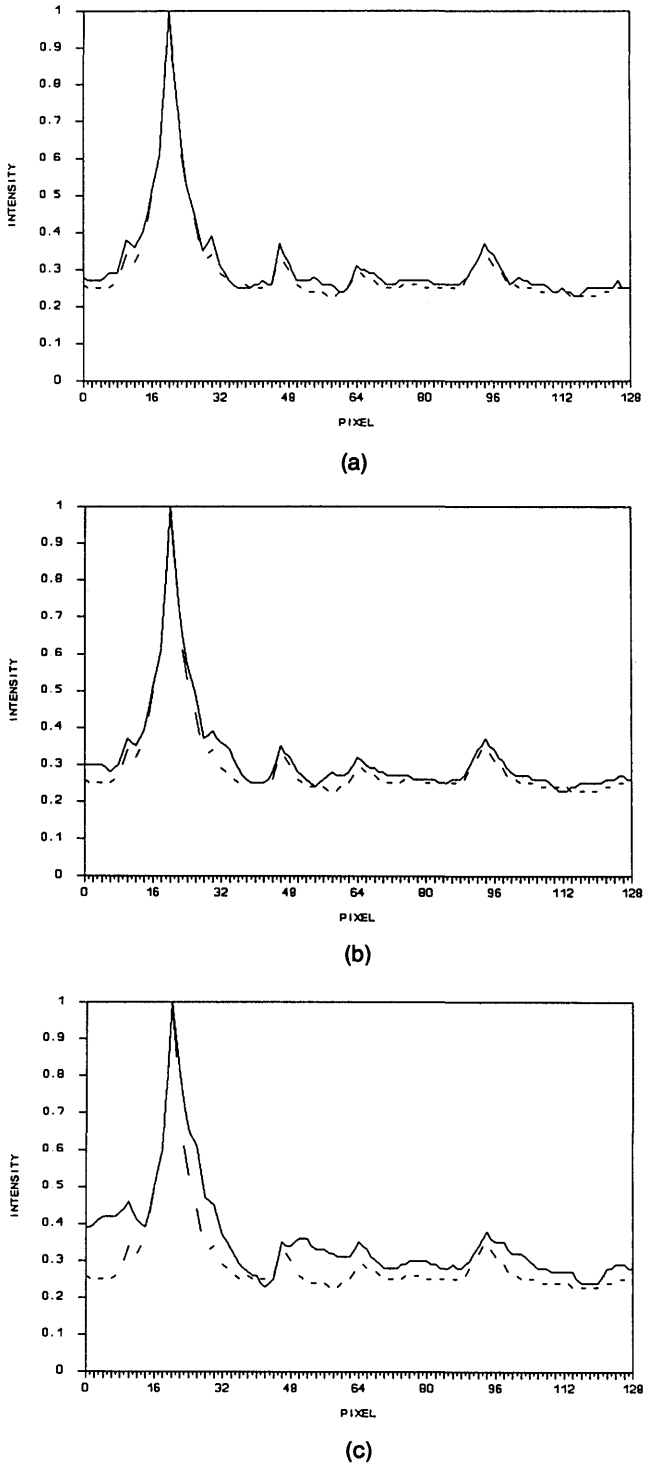

Fig. 2. Reconstructions (continuous curves) of the object of Fig. 1 with different amounts of noise added to the spectrum [here the object (dashed curves) is the CCD row without background and bias substraction]: (a) SNR = 20, (b) SNR = 10, (c) SNR = 5 (these values are averaged over the whole spectrum).

Table 1. Initial and Final Cost Functions for the Different Noise Levels

SNR	Initial Cost Function	Final Cost Function
∞	7.5×10^{-2}	2.0×10^{-5}
20	8.0×10^{-2}	1.3×10^{-3}
10	9.3×10^{-2}	3.3×10^{-3}
5	1.0×10^{-1}	7.6×10^{-3}

curves; these are the CCD images of M51 without bias and background subtraction) with these SNR values. Here the algorithm was composed of the initial ER cycle followed by three hybrid cycles, each with 50 HIO and 10 ER iterations (two hybrid cycles were enough for the case SNR = 20). Table 1 shows a comparison of the initial and final cost functions of the reconstructions, including the noiseless case (SNR = ∞). The last reconstruction (SNR = 5) has been smoothed by a slightly low-pass filter to decrease the reconstruction noise. This smoothing provides a better-appearing image.

The three reconstructions show the major features of the object, but, as the noise level increases, the low-intensity structures are progressively embedded in noise. On the other hand, when the SNR is halved, the value of the resulting cost function is roughly duplicated, as Table 1 shows. Such an inverse proportionality suggests a sort of linear transmission of the noise from the spectra to the reconstructed image. This also suggests that the convergence of the algorithm is not strongly affected by noise but that a similar image quality could be obtained if one knew the actual but noisy phase of the FT of the object.

4. IMAGE RECONSTRUCTION FROM COMPUTER-SIMULATED ONE-DIMENSIONAL INFRARED STELLAR SPECKLE INTERFEROMETRY

In this section we study the performance of the method as applied to infrared 1-D SSI by a realistic computer simulation. The main difference between visible and infrared SSI is that in the former the noise is Poissonian (correlated with the signal), whereas in the infrared range the additive background noise is dominant.[14] In the computer simulation, the noise was not generated by a computer. Instead, actual background measurements (see Section 5 below) were added to the speckle images.

A. Computer Generation of Speckle Images

The method used in the generation of short-exposure images has already been described[15] (it was applied to the photon-limited 2-D case). To generate 1-D speckle images we followed the same method, with the sole difference of final integration over the Y axis. In this way we can simulate the integrating effect of a scanning slit, preserving the 2-D nature of the image-formation process. The method basically consists of two steps: First, a set of random numbers, with negative exponential probability distribution, is modulated by the FT of the Fried short-exposure modulation transfer function[16] (MTF). The resulting set is a speckle image of a point source (PSF), with a sampling interval of 1 pixel/speckle grain. Then the pupil phase is estimated by a few iterations with the Gerchberg–Saxton algorithm.[17] Once the pupil function is obtained, the speckle image can be recomputed to obtain the desired sampling ratio (2 pixels/speckle in what follows). Finally, short-exposure images of an extended object are obtained by convolving the object with each short-exposure PSF. The object was that of Fig. 1.

In this simulation we wanted to approximate as much as possible the experimental conditions of our observations (see Section 5 below). We have assumed imaging through a 1.5-m telescope and a wavelength of 2.2 μm, which yields a theoretical resolution of roughly 0.3 arcsec. The seeing disk is assumed to be 2 arcsec. The size (width to half-height) of the resulting long-exposure PSF (the seeing disk) was 13 pixels. Both point and extended speckle images were computed inside a window of 128 × 128 pixels. The final window was 128 × 1 pixels after integration over the Y axis. In the infrared range, the background (additive) noise dominates over the Poissonian photon noise.[14] Thus we have assumed only background noise. We used actual background observations of IRC +10216 as the additive background noise, rescaled to obtain the desired SNR in each speckle image. The SNR is considered here the integrated energy of the signal, over the 128 pixels of each speckle image, divided by that of the background. We present simulations corresponding to two different values of the background noise: 2% and 5%, which are close to the values found in our observations of IRC +10216. The noise was added to both point and extended object speckle images. Finally, 50 speckle images of each type were generated and used in each simulation.

B. Stellar Speckle Interferometry Exponential Filtering and Deconvolution

Once the speckle images were generated, SSI was carried out by computing the average power spectra of both sets of PSF and object images. Also, we computed the average power spectrum of a set of background images, $\langle N_k(u)|^2\rangle$. Then each speckle image, and also each background image, was multiplied by the exponential filter $g(x) = \exp(\alpha x)$, with $\alpha = 0.015$ ($\alpha L_x = 1.92$), and the same procedure was repeated with the filtered images.

Before deconvolving the image by the PSF, it is usual in infrared SSI to substract the power spectrum of the background from the power spectrum of the signals. Since we have assumed the presence of only background noise (infrared), in the 1-D case (Eq. 1) becomes

$$i_k(x) = o(x) * p_k(x) + n_k(x), \tag{5a}$$

where $n_k(x)$ is the background noise. In terms of the average power spectra it can be written as

$$\langle|I_k(u)|^2\rangle = |F(u)|^2\langle|P_k(u)|^2\rangle + \langle|N_k(u)|^2\rangle. \tag{5b}$$

Here, the cross term $\langle 2\,\mathrm{Re}[F(u)P_k(u)N_k(u)]\rangle$ has been neglected. This term is likely to be close to zero since both $P_k(u)$ and $N_k(u)$ oscillate randomly, taking positive and negative values. The average tends to be zero in the same way that the long-exposure MTF is zero for high frequencies. Anyway, Eq. (5b) is approximate and could fail in the presence of too much noise. To solve Eq. (5b), we applied a Wiener filter. This filter is useful to deconvolve noisy signals, because it regularizes the deconvolution depending on

the SNR at each frequency. The final expression for the estimate of the modulus of the FT of the object, $|F(u)|$, by Wiener filtering when the noise is additive,[18,19] including the background substraction, becomes

$$|F(u)| = [\langle |I_k(u)|^2 \rangle - \langle |N_k(u)|^2 \rangle]^{1/2} \frac{[\langle |P_k(u)|^2 \rangle]^{1/2}}{\langle |P_k(u)|^2 \rangle + \langle |N_k(u)|^2 \rangle}, \quad (6)$$

where it has been assumed that the background noise of the PSF images is negligible. In general, the background power spectrum should also be substracted from $\langle |P_k(u)|^2 \rangle$. Note that the first term on the right-hand side of Eq. (6) is the modulus of the FT of the image, corrected from background, whereas the second term is the Wiener filter. In practice, the power spectrum of the background $\langle |N_k(u)|^2 \rangle$ is highly irregular (noisy); thus it is useful to substitute for it a monotonic function (e.g., a polynome or a theoretical model) by some curve fitting (we used a four-order polynomial fit). The SNR of the power spectrum in both cases was greater than 1, being ~1.7 at 75% of the cutoff frequency in the noisiest case. On the other hand, it can also be convenient to substitute for $\langle |P_k(u)|^2 \rangle$ a curve fitting of the data to the MTF of a model such as that of Korff[20] or Dainty.[2] We applied these fits and obtained better results in the deconvolutions.

Equation (6) also applies for the exponential filtered images by substitution of F', I', P', and N', for F, I, P, and N, respectively. Then, by applying Eq. (6) twice, we obtained optimum (the Wiener filter is the optimum filter in a least-squares sense) estimates of $|F(u)|$ and $|F'(u)|$.

C. Reconstructions

The modified Walker algorithm was applied to obtain the reconstructions shown in Figs. 3(a) and 3(b), corresponding to 2% and 5%, respectively, of background noise. The reconstructions were achieved by the same procedure described in Subsection 3.B. Two hybrid cycles were applied to the 2% background noise simulation, whereas three cycles were needed to obtain the result with 5% noise. The final cost functions were 4.2×10^{-3} and 6×10^{-3}, respectively. The reconstructions show two effects, when compared with the original, that increase with the amount of noise: First, there is a slight resolution loss because of the Wiener filter. The reconstructions are smoothed because the filter decreases the high frequencies as the noise increases. On the other hand, the second effect is that the low-level intensity features are embedded in noise. This effect is similar to that found in the reconstructions described in Subsection 3.B (see Fig. 2), but now even the noise is smoothed by the Wiener filter. However, our main conclusion is that the method studied above is able to yield good results with some limitations imposed by the amount of noise. It follows from our simulation results that whenever the SNR of the power spectrum is greater than 1 for all frequencies, a reasonably good reconstruction may be expected. We have mentioned that our aim was to simulate experimental conditions in a realistic way. In fact, data such as the background noise level, the number of speckle images, the seeing, and the telescope diameter of this simulation are inspired by, and in consequence are close to, the experimental data presented in Section 5.

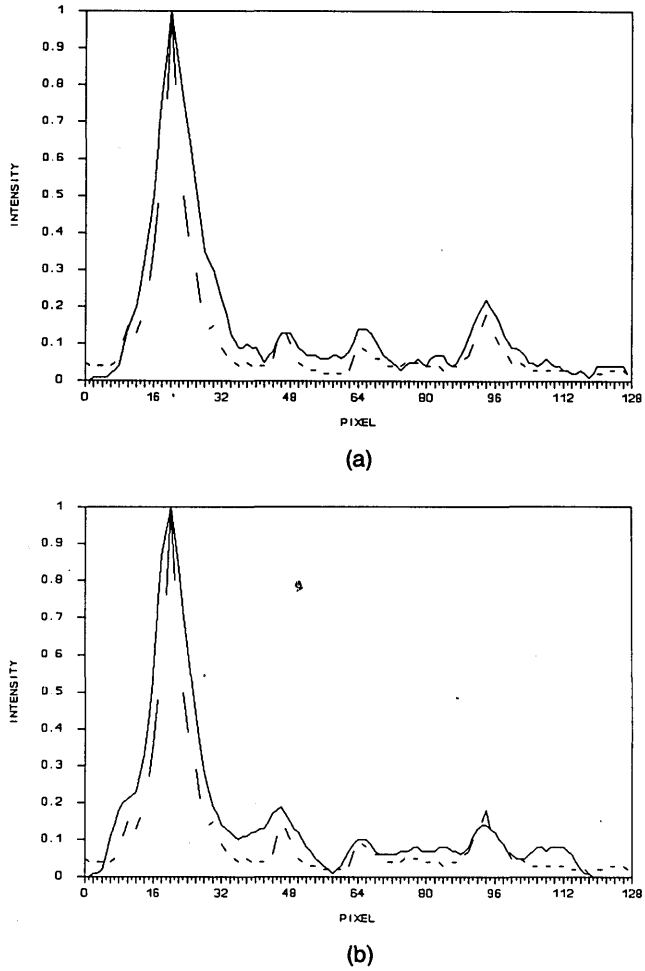

Fig. 3. Reconstructions from computer-simulated infrared SSI (results are shown by continuous curves; the object is shown by dashed curves): (a) background noise of 2% (in each specklegram), (b) background noise of 5%.

5. RECONSTRUCTION OF THE SOURCE IRC +10216

IRC +10216 is the brightest extrasolar source in the 5-μm band. Since it is also an extended object, it constitutes an excellent test for near-infrared high-resolution imaging. Although its geometry is not well known today, there is some agreement that it seems to be a normal-luminosity carbon star surrounded by a circumstellar shell. Several high-resolution 1-D infrared observations have been reported (see, for instance, Refs. 21–23). Also, 1-D object reconstructions of IRC +10216 by the Knox–Thompson method have been reported by Dyck *et al.*[24] Their reconstructions, in the 2.2-μm band, show a clear departure from the circular symmetry in the north–south direction, with an extended wing on the north side. On the contrary, their results at 10.3 μm were clearly symmetric. They explained these results by assuming a bipolar model including a circumstellar shell and an extended opaque equatorial disk.

A. Experimental Data and Methods

In what follows, we present results of observation of IRC +10216 in two near-infrared wavelengths, corresponding to the K (2.2 μm) and M (4.94 μm) photometric bands. Obser-

vations were made with the 1.5-m Carlos Sánchez Magro Telescope at the Observatorio del Teide (Canary Islands) on March 6 and 7, 1984.[25] Specklegrams were obtained by an InSb single detector placed behind a scanning slit (30 μm wide, corresponding to 0.3-arcsec angular resolution). Specklegrams of μ UMa and α Ori were also obtained as references for the K and M bands, respectively. The scans were made in the north–south and east–west directions. Also, background scans were taken with both K and M filters.

The 50 best specklegrams of each set were selected for computation of the average power spectra of the images, with and without an exponential filter. We applied the same procedure as that used with the simulation described in Section 4 to obtain the final estimate of the object spectra and reconstructions. The sole difference is that here the MTF, $\langle |P_k(u)|^2 \rangle^{1/2}$, was corrected from the scanning slit by dividing it by the MTF of the slit. On the other hand, the MTF for each band was fitted to the Korff[20] and Dainty[2] models. In this way, a 1.8-arcsec seeing disk was obtained in K (r_0 = 25.2 cm). In the M band, the fitting gave a seeing disk of 2.86 arcsec. The diffraction cutoff frequencies of the 1.5-m telescope are 3.22 cycles/arcsec (0.32-arcsec resolution) in K and 1.47 cycles/arcsec (0.68-arcsec) in M. In Figs. 4–11 the spatial frequency will appear normalized with respect to the corresponding cutoff frequency. On the other hand, the average spectra were greater than zero within a window of 100 pixels in K and 120 in M. In that case the maximum number of resolvable pixels of the object would be 50 and 60, respectively, by the sampling theorem (the effective number of resolvable pixels in M is, in fact, fewer than 30 because of oversampling). As a consequence, the parameter of the exponential filter was set to $\alpha = 0.03$. Figure 4(a) shows the experimental speckle MTF in the K band (continuous curve) compared with the result of the Korff fitting (symbols). The MTF corresponding to the M filter is shown in Fig. 4(b). In the latter case, the symbols show the fitting to the Dainty model (this model is simpler than Korff's, but at the cost of a worse fit to the experimental data). Figure 5 shows a polynomial fitting of the ratio of the average power spectra of the background scans versus the signal scans for both K and M filters. This ratio is useful for estimating the influence of the background noise. Also, we applied these fittings to the background subtraction and deconvolution instead of directly using the noisy background average power spectrum. This procedure improved the quality of the results.

B. Results

The east–west scans were not resolvable by our telescope in either the K or the M band, i.e., the power spectra could not be distinguished from those of the reference sources in that direction. In consequence, we did not try the reconstructions. The north–south scans, on the contrary, clearly show structure after deconvolution. Figures 6(a) and 6(b) show the estimated power spectra of IRC +10216 in the K and M photometric bands, respectively, after background substraction and Wiener deconvolution [Eq. (6)]. Because the source is so bright, the SNR of the spectra at 75% of the cutoff frequency is roughly 10 in K and 4 in M. These values are even better than those of the computer simulation given in Section 4. In consequence, good-quality reconstructions are expected.

The north–south reconstructions are shown in Fig. 7 for the K band and in Fig. 8 for M. The reconstruction of Fig. 7 could be obtained even with a fast version of the algorithm: 10 ER iterations plus two cycles, each one composed of 5 HIO followed by 2 ER algorithms. This is surely due to the

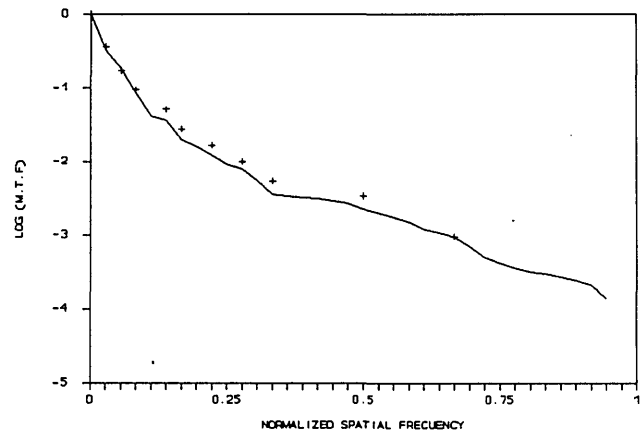

(a)

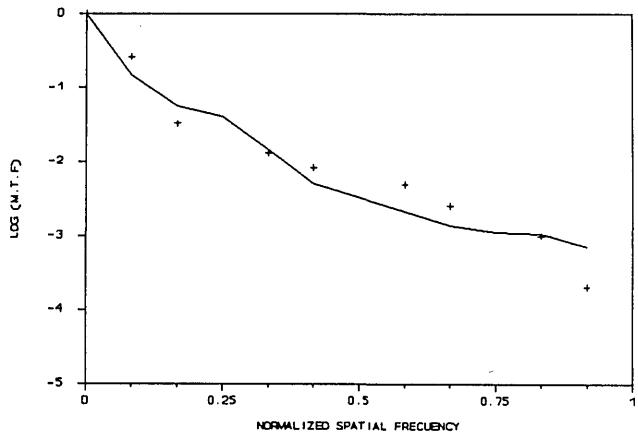

(b)

Fig. 4. Average power spectra of the two reference stars, i.e. the power MTF (logarithmic scale): (a) MTF in the K (2.2-μm) band; the symbols represent the fitting to the Korff model. (b) MTF in the M (5-μm) band; here the symbols show the Dainty model fitting.

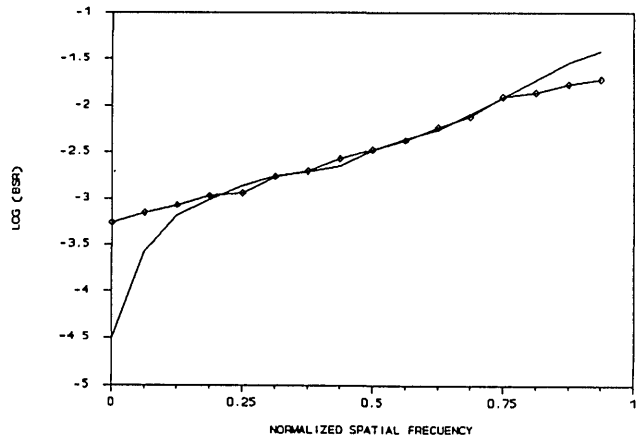

Fig. 5. Polynomial fitting of the ratio of the average power spectra of the background-versus-signal specklegrams. K and M are represented without and with symbols, respectively (logarithmic scale).

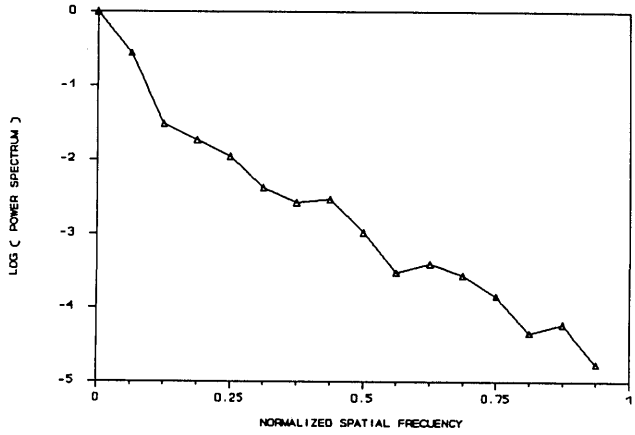

(a)

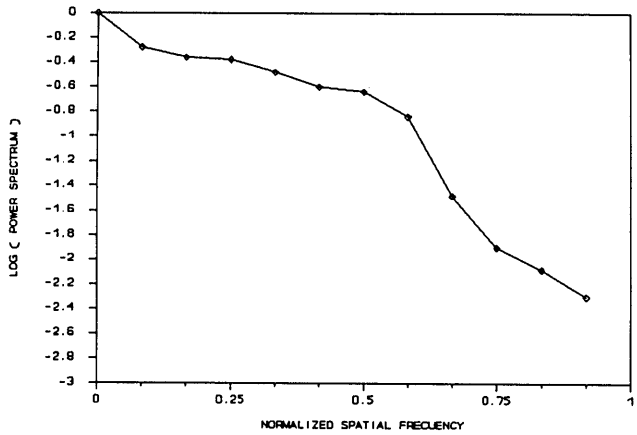

(b)

Fig. 6. Resulting estimate of the power spectra, corresponding to (a) the K and (b) the M bands, after Wiener filtering deconvolution and background substraction (logarithmic scale).

small number of pixels, 50, of the object and makes the convergence much better and easier than with the 128-pixel object of the computer simulation. The final cost function was approximately 10^{-4}, which is more than an order of magnitude better than those given in Section 4. The reconstruction (Fig. 7) shows three unresolvable components, with the peaks placed at 1.5, 2.3, and 2.9 arcsec from the origin of coordinates (north side), which have increasing luminosity. These components seem to emerge from a circumstellar extended shell, more than 4 arcsec wide. Although the central component is placed close to the center of the shell, there is no symmetry, since the three components have different luminosities. These results seem to be in agreement with those of Dyck *et al.*,[23] who needed a three-Gaussians model to fit their spectrum.

Figure 8 shows the reconstruction of IRC +10216 made with the M photometric filter. In this case the final cost function was 5×10^{-4}. This value is somewhat worse than that we obtained in K, mainly due to the smaller value of the SNR (however, the cost function is better than those of Section 4). The M reconstruction shows a main unresolvable component having a wing on the north side. This result has the same shape and orientation, but double the width, as that found by Dyck *et al.*[24] in the K band after reconstruction by the Knox–Thompson method.

C. Discussion

Our results seem, to some extent, to be compatible with those of some previous authors.[23,24] However, some discrepancies exist among published data, mainly with respect to the number of components. On the other hand, there is evidence suggesting that this source is variable, which could explain such discrepancies. In consequence, we concentrate here on analyzing the compatibility of our two reconstructions, K and M, with respect to each other and with shift-and-add results obtained with the same data.

A superposition of K and M reconstructions is shown in Fig. 9. The two results appear to be compatible, since the M reconstruction could roughly be interpreted as a low-pass-filtered version of the K reconstruction. The main difference, apart from different resolutions (a factor of 2, approximately), which is clear at first sight, is an important relative luminosity loss of the circumstellar shell: in 5 μm as opposed to 2.2 μm. However, a plausible explanation could be that there is an important relative increment of the luminosity of the central components in 5 μm, while the circumstellar shell does not experience the same increment. Other features of the source, such as the spatial distribution, orientation, and size, are the same in both K and M reconstructions, except for double resolution in the former.

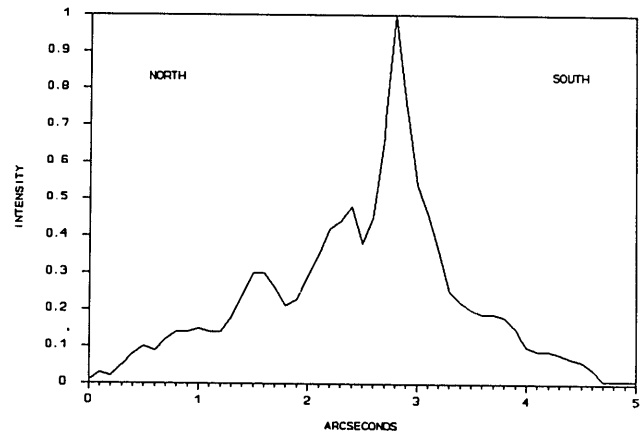

Fig. 7. Reconstruction of a north–south scan of IRC +10216 in the K photometric band. It shows three components inside a circumstellar shell.

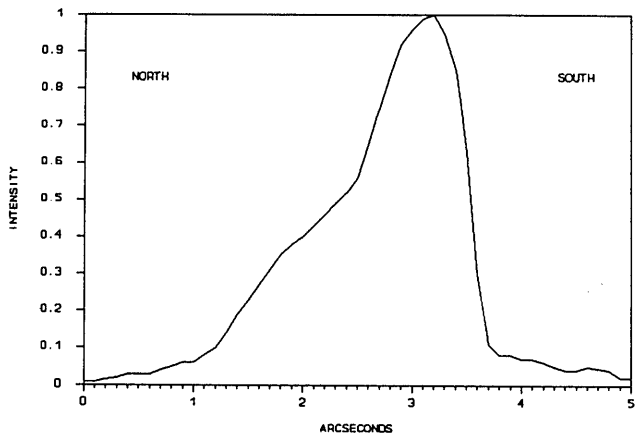

Fig. 8. Reconstruction in the M band. Here, the structure consists of a main component with a wing on the north side.

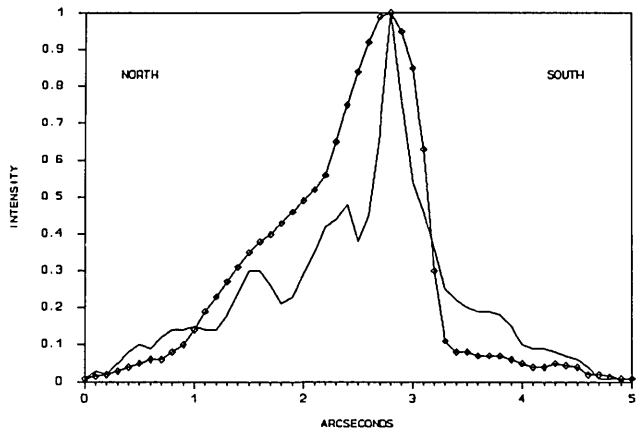

Fig. 9. Comparison of K and M (symbols) reconstructions. There are two main differences: in M the resolution is approximately twice as bad, and the circumstellar shell has a lesser relative intensity.

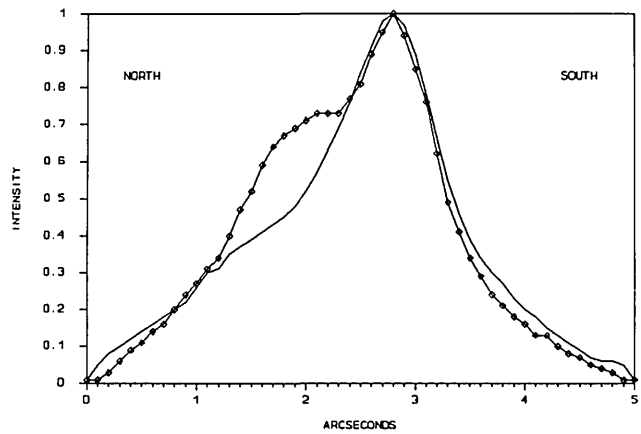

Fig. 10. Comparison for the K band of the result obtained with (symbols) shift-and-add and (curve without symbols) a low-pass-filtered version of the reconstruction.

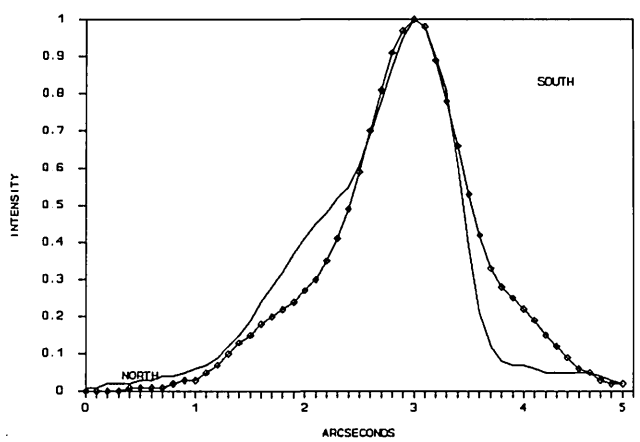

Fig. 11. Shift-and-add (symbols) in M compared with the exponential filtering reconstruction (here the reconstruction has been represented without low-pass filtering).

The second step in testing our results was to compare the reconstructions with shift-and-add results of the same data. This method was carried out by shifting the specklegrams in order to place the brightest speckle grain (in fact, the brightest pixel) in the central pixel. Once all the specklegrams are recentered, they are averaged to obtain the image. Figures 10 and 11 show for K and M, respectively, a comparison between the shift-and-add result (symbols) and the reconstruction (continuous curves). In Fig. 10, corresponding to K, the reconstruction has been convolved with a low-pass filter. The low pass is used here to equalize resolutions, since the shift-and-add method gives an intermediate resolution between speckle interferometry and direct imaging, depending on the ratio of the telescope diameter to the Fried parameter. The M reconstruction appears in Fig. 11 without filtering, since the resolution is similar in this case. The two comparisons, K and M, show opposite behavior for the north side wing. In K, shift-and-add gives a wing more pronounced than that of the low-pass reconstruction. In M, the contrary occurs. In the second case, there are differences in both north and south sides (see Fig. 11). At the north side, the shift-and-add wing is almost undistinguishable, whereas at the south side the intensity decay is much smoother. However, the application of a slight low-pass filter to the M reconstruction permitted a much better coincidence with shift-and-add. (By looking at the low-pass version of the K reconstruction shown in Fig. 10, one can deduce that both the north side wing and the south side steep decay will be smoothed by the low-pass filter, leading to coincidence with the shift-and-add result of Fig. 11.) The remaining disagreement between the shift-and-add and reconstruction results consists in the different relative intensities of the north side wing in K (Fig. 10). However, that could also be explained in terms of a relative intensity loss of the main peak caused by the shift-and-add method. In fact, this kind of minor discrepancy in the appearance of the shift-and-add results and low-pass reconstructions should be attributed to the different shapes of the PSF's resulting from the two methods when the Wiener filtering that was applied before the reconstructions is taken into account.

6. SUMMARY

We have presented different results of 1-D image reconstruction by exponential filtering. This has been done in three steps. First, an improved version of the Walker algorithm was proposed, based on the combination of the two versions (ER and HIO) of the Fienup algorithm. The second step was to show the good performance of this method when it was applied to the 1-D case. We found that exponential filtering, with the improved algorithm, was always able to give the correct reconstruction in all noiseless cases (we tested objects as much as 300 pixels wide). Then the method was tested, first with increasing amounts of random noise added to the spectra and then with a realistic computer simulation of 1-D infrared speckle interferometry. In both cases we could see the great influence of noise, whose main effect was the appearance of noise in the reconstruction rather than convergence problems.

Finally, the method was applied to reconstruct 1-D scans of the source IRC +10216 in two near-infrared photometric bands, K (2.2 μm) and M (5 μm). The north–south recon-

struction in the K band clearly shows three components, which are surrounded by a circumstellar shell. In M, however, the shell had relatively less intensity, and only a wing on the north side of the main component was detected, because of less resolution. A low-pass version of these results was compared with shift-and-add scans obtained from the same data, showing that both are compatible.

ACKNOWLEDGMENTS

The authors thank J. J. Fuensalida, who provided us the experimental data (specklegrams) and M. Nieto-Vesperinas for his useful suggestions. This research has been supported by the Comisión Interministerial de Ciencia y Tecnología and the Instituto de Astrofísica de Canarias.

REFERENCES

1. A. Labeyrie, "Attainment of diffraction limited resolution in large telescopes by Fourier analyzing speckle patterns in a star image," Astron. Astrophys. **6,** 85–87 (1970).
2. J. C. Dainty, "Stellar speckle interferometry," in *Laser Speckle and Related Phenomena,* 2nd ed., J. C. Dainty, ed. (Springer-Verlag, Berlin, 1984), pp. 255–320.
3. Y. M. Bruck and L. G. Sodin, "On the ambiguity of the image reconstruction problem," Opt. Commun. **30,** 304–308 (1979).
4. M. H. Hayes and J. M. McClellan, "Reducible polynomials in more than one variable," Proc. IEEE **70,** 197–198 (1982).
5. A. Walther, "The question of phase retrieval in optics," Opt. Acta **10,** 41–49 (1963).
6. K. T. Knox and B. J. Thompson, "Recovery of images from atmospherically degraded short-exposure photographs," Astrophys. J. Lett. **193,** L45-L48 (1974).
7. A. W. Lohmann, G. P. Weigelt, and B. Wirnitzer, "Speckle masking in astronomy: triple correlation theory and applications," Appl. Opt. **22,** 4028–4037 (1983).
8. J. G. Walker, "The phase retrieval problem: a solution based on zero location by exponential apodization," Opt. Acta **28,** 735–738 (1981).
9. J. G. Walker, "Computer simulation of a method for object reconstruction from stellar speckle interferometry data," Appl. Opt. **21,** 3132–3137 (1982).
10. J. R. Fienup, "Reconstruction of an object from the modulus of its Fourier transform," Opt. Lett. **3,** 27–29 (1978).
11. M. Nieto-Vesperinas, R. Navarro, and F. J. Fuentes, "Performance of a simulated-annealing algorithm for phase retrieval," J. Opt. Soc. Am. A **5,** 30–38 (1988).
12. J. R. Fienup, "Phase retrieval algorithms: a comparison," Appl. Opt. **21,** 2758–2769 (1982).
13. J. C. Dainty and J. R. Fienup, "Phase retrieval and image reconstruction for astronomy," in *Image Recovery: Theory and Application,* H. Stark, ed. (Academic, New York, 1987) pp. 231–275.
14. F. Sibille, A. Chelli, and P. Lena, "Infrared speckle interferometry," Astron. Astrophys. **79,** 315–328 (1979).
15. R. Navarro, F. J. Fuentes, and M. Nieto-Vesperinas, "Simulated annealing image reconstruction in photon-limited stellar speckle interferometry," Astron. Astrophys. **208,** 374–380 (1989).
16. D. L. Fried, "Limiting resolution looking down through the atmosphere," J. Opt. Soc. Am. **56,** 1380–1384 (1966).
17. R. W. Gerchberg and W. O. Saxton, "A practical algorithm for the determination of phase from image and diffraction plane pictures," Optik **35,** 237–246 (1972).
18. J. W. Brault and O. R. White, "The analysis and restoration of astronomical data via the fast Fourier transform," Astron. Astrophys. **13,** 169–189 (1971).
19. W. K. Pratt, *Digital Image Processing* (Wiley, New York, 1978).
20. D. Korff, "Analysis of a method for obtaining near-diffraction-limited information in the presence of atmospheric turbulence," J. Opt. Soc. Am. **63,** 971–980 (1973).
21. M. J. Selby, R. Wade, and C. Sánchez Magro, "Speckle interferometry in the near-infrared," Mon. Not. R. Astron. Soc. **187,** 533–566 (1979).
22. J. M. Mariotti, A. Chelli, R. Foy, P. Lena, F. Sibille, and G. Tchountonov, "Infrared speckle imaging: improvement of the method: results on Miras and protostars," Astron. Astrophys. **120,** 237–248 (1983).
23. H. M. Dyck, B. Zuckerman, Ch. Leinert, and S. Beckwith, "Near-infrared speckle interferometry of evolved stars and bipolar nebulae," Astrophys. J. **287,** 801–813 (1984).
24. H. M. Dyck, B. Zuckerman, R. R. Howell, and S. Beckwith, "Measurements of the circumstellar shell geometry in IRC +10216," Publ. Astron. Soc. Pac. **99,** 99–106 (1987).
25. J. J. Fuensalida, "Alta resolución espacial en el infrarrojo cercano," Ph.D. dissertation (University of La Laguna, Tenerife, Spain, June, 1986).